Lab on a Chip

PAPER

View Article Online
View Journal

Cite this: DOI: 10.1039/c7lc00740j

Cardiac microphysiological devices with flexible thin-film sensors for higher-throughput drug screening†

Johan U. Lind,[a] Moran Yadid,[a] Ian Perkins,[a] Blakely B. O'Connor,[a] Feyisayo Eweje,[a] Christophe O. Chantre,[a] Matthew A. Hemphill,[a] Hongyan Yuan,‡[a] Patrick H. Campbell,[a] Joost J. Vlassak[b] and Kevin K. Parker *[a]

Received 16th July 2017,
Accepted 22nd September 2017

DOI: 10.1039/c7lc00740j

rsc.li/loc

Microphysiological systems and organs-on-chips promise to accelerate biomedical and pharmaceutical research by providing accurate *in vitro* replicas of human tissue. Aside from addressing the physiological accuracy of the model tissues, there is a pressing need for improving the throughput of these platforms. To do so, scalable data acquisition strategies must be introduced. To this end, we here present an instrumented 24-well plate platform for higher-throughput studies of engineered human stem cell-derived cardiac muscle tissues that recapitulate the laminar structure of the native ventricle. In each well of the platform, an embedded flexible strain gauge provides continuous and non-invasive readout of the contractile stress and beat rate of an engineered cardiac tissue. The sensors are based on micro-cracked titanium–gold thin films, which ensure that the sensors are highly compliant and robust. We demonstrate the value of the platform for toxicology and drug-testing purposes by performing 12 complete dose–response studies of cardiac and cardiotoxic drugs. Additionally, we showcase the ability to couple the cardiac tissues with endothelial barriers. In these studies, which mimic the passage of drugs through the blood vessels to the musculature of the heart, we regulate the temporal onset of cardiac drug responses by modulating endothelial barrier permeability *in vitro*.

Introduction

The staggering costs associated with drug development limit innovation and render cutting-edge therapies unattainable for countless patients. The limited efficiency of traditional preclinical models to identify toxic or ineffective compounds is a key part of this issue.[1,2] Thus, retrospective analyses have found that merely ~50% of rodent studies are predictive of human toxicity.[3] The potential of organs-on-chips and microphysiological systems (MPS) is that *in vitro* engineered tissues based on human stem cells will provide more predictive preclinical drug assessments, at a lower cost. Since heart failure remains a leading cause of death and cardiotoxicity is one of the most prevalent causes of drug withdrawal,[4] tools for modeling the human cardiac musculature are of particular interest.

A central challenge for any microphysiological system is to faithfully recapitulate structural and functional hallmarks of the native tissue counterpart. In the mammalian heart, numerous sheets of highly aligned muscle cells wrap circumferentially around the heart chambers, following a spiraling angle from the epi- to the endo-cardium.[5,6] Notably, each muscle layer merely spans approximately 4 cells in thickness, with each layer being spaced by the extensive connective tissue in the heart.[7] Muscular thin film (MTF) platforms mimic this laminar architecture in the form of engineered anisotropic 2D muscle tissues on soft material cantilever substrates.[8–10] Upon muscle tissue contraction, the cantilever bends proportionally to the stress generated by the tissue. By optically tracking cantilever motion in a microscope setup, changes in contractile stress can be quantified, enabling drug testing and disease modeling.[11,12] However, the reliance on optical tracking as readout creates obstacles for scaling the assay to real-time and higher-throughput formats, as optical readouts are data-heavy, often require post-processing and are hardware intensive.

In this report, we present a multi-well cardiac MTF platform with integrated flexible strain gauges. The sensors are

[a] *Disease Biophysics Group, John A. Paulson School of Engineering and Applied Sciences, Wyss Institute for Biologically Inspired Engineering, Harvard University, 29 Oxford St., Pierce Hall 321, Cambridge, Massachusetts 02138, USA. E-mail: kkparker@seas.harvard.edu; Fax: +(617) 495 9837; Tel: +(617) 495 2850*
[b] *John A. Paulson School of Engineering and Applied Sciences, Harvard University, Cambridge, Massachusetts 02138, USA*

† Electronic supplementary information (ESI) available. See DOI: 10.1039/c7lc00740j

‡ Current affiliations: Department of Mechanical, Industrial and Systems Engineering, University of Rhode Island, Kingston, RI, 02881, USA.

based on robust and compliant micro-cracked gold thin films, which can readily be deformed by the small stresses exerted by the engineered cardiac muscle tissue. The platform provides continuous electronic readout of the contractile stress and beat rate of up to 24 separate cardiac tissues. The electronic readout streamlines experimentation and data acquisition, which we demonstrate by performing dose–response studies of 12 cardiac drugs on human induced pluripotent stem cell-derived cardiomyocyte (hiPS-CM) tissues. Additionally, the open-well format of the platform allows us to easily couple the cardiac MTFs with endothelial barrier inserts, and study the temporal drug transport across the barriers. We take advantage of this to mimic the changes in cardiac drug transport across the vasculature endothelium that occurs during inflammation, by exposing the endothelial barriers to TNF-α.[13–16]

Results & discussion

Device principle & engineered cardiac tissues

The central part of the device is a ~25 μm thick, multilayer poly(dimethylsiloxane) (PDMS)-based cantilever that combines control of tissue structure with electronic readout of the contractile function; see Fig. 1. On the surface of each cantilever is an engineered, cardiac thin film tissue, based on either hiPS-CMs or neonatal rat ventricular myocytes (NRVM). Upon tissue contraction and shortening, the underlying PDMS cantilever is bent and a flexible titanium–gold thin-film strain gauge, embedded in the cantilever, is strained. This generates an increase in resistance proportional to the tissue contractile stress; see Fig. 1a and b. We recently introduced this general principle in a lower-throughput device that relied on highly specialized 3D-printing equipment for fabrication.[17,18] In addition to significantly increasing the throughput, we here focused on designing a generally accessible platform, by basing device manufacture on more commonly available and scalable tools. To this end, we applied sequential spin-coating to fabricate the bulk of the stacked PDMS cantilever structure and used a CO_2 laser cutter to define the cantilevers.[12] Spin coating provided a facile method for deposition of multiple PDMS layers, each in the μm range. Similarly, e-beam evaporation was applied to create titanium–gold thin-film strain gauges. The fabrication procedure is outlined in Fig. S1.†

The architecture of the tissues was engineered to recapitulate the laminar structure and anisotropy of native cardiac musculature, following principles described in our previous reports.[8,10,18] To develop hiPS-CM tissues, we used microgrooves molded in 500 kPa PDMS. Groove barriers were 5 μm tall and 4 μm wide and were coated with fibronectin (FN) prior to cell seeding; see Fig. 1c and d. Culturing hiPS-CMs on the molded substrates gave rise to tissues with highly aligned sarcomeres; see Fig. 1e. Correspondingly, the hiPS-CM tissues displayed a sarcomeric organizational order parameter (OOP)[19] of 0.31; see Fig. S2.† For NRVM-based tissues, we used micro-contact printing to apply FN line

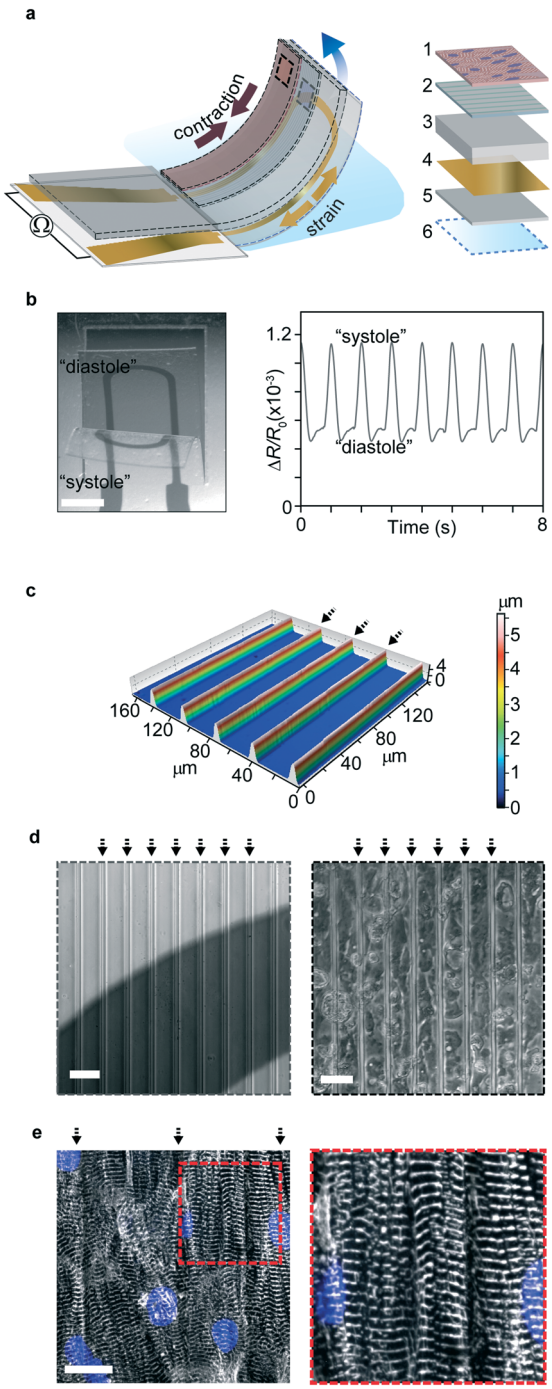

Fig. 1 Engineered cardiac muscle tissue on cantilever with embedded flexible thin-film strain gauge. (a) Principle sketch of device cantilever and constituent layers 1: engineered cardiac muscle tissue 2: tissue-aligning micro-molded or micro-patterned layer 3: PDMS layer, 4: Ti–Au thin-film sensor layer, 5: bottom PDMS layer 6: PNIPAAM release layer. (b) Example optical micrograph of a deflecting cantilever and corresponding electrical readout, scale bar 1 mm. (c) Optical profilometer characterization of molded 500 kPa PDMS surface. Arrows indicate barrier peaks. (d) Left: Bright field optical micrograph of grooves on cantilevers applied for structural guidance of hiPS-CM tissues, strain gauge wire seen a dark area. Right: Bright field optical micrograph of hiPS-CM tissue on molded PDMS top layer, scale bars 40 μm. (e) Confocal microscopy of immunostained hiPS-CM tissue, blue: DAPI nuclei stain, white α-actinin. Scale bar 20 μm.

patterns and generate anisotropic engineered tissues, as previously described.[8,12] The OOP for NRVM tissues was 0.40; see Fig. S2.† Both classes of tissues further displayed electrical connectivity through gap junctions; see Fig. S3 and S4.† The engineered tissues thus replicate essential structural hallmarks of the musculature of the heart.

Micro-cracked titanium–gold thin films as sensor material

To achieve reliable device fabrication and readout, it was essential to limit the overall thickness of each layer of the cantilever, and of the titanium–gold strain gauge sensors in particular. Metal thin films can be deposited consistently in the nanometer range using e-beam evaporation, providing a robust route to sensor fabrication. Yet, beyond limiting the sensor thickness, we found that it was crucial to control the thin-film micro-structure. The Ti–Au thin films were deposited on thin ~5 μm PDMS substrates, which constitute the bottom part of the final cantilevers. We initially observed that macroscopic cracks occurred frequently and spontaneously when applying Ti adhesion layers of thicknesses 5 nm and greater on these μm thin PDMS substrates; see Fig. 2a. Such macroscopic cracks commonly led to discontinuities and device failure. We subsequently noted that these macroscopic cracks did not occur when reducing the Ti adhesion layer thickness to 3 nm. SEM imaging revealed that this corresponded to a transition in the micro-structure of the Ti–Au thin-films from micro-buckled to micro-cracked;[20,21] see Fig. 2a. In accordance with previous findings, the micro-cracked thin films were highly stretchable, allowing strains in excess of 10% without failure;[20,22] see Fig. 2b. We attribute the absence of macroscopic cracks in the micro-cracked thin films to their ability to withstand large strains by deforming out of plane. In addition to overcoming macroscopic failures, the micro-cracked thin films gave rise to reliable signals with negligible dependency on rate in the 0.1% strain regime that was found to be relevant for the final device; see Fig. 2c. Also, no notable changes in baseline resistance were detected during week-long tissue culture. Hence, the micro-cracked Ti–Au thin films provide a robust basis for the instrumented MTF cantilevers.

The thickness of the titanium adhesion layer has previously been reported to have a pronounced effect on the micro-structure of titanium–gold thin films deposited on PDMS substrates.[21] In previous reports, adhesion layers thicknesses of up to 6 nm, as compared to the 3 nm observed here, were reported to give rise to micro-cracked structures.[21] Surprisingly, we found that the threshold below which micro-cracking occurs depends on PDMS substrate thickness. When increasing the PDMS substrate thickness above the 5 μm used in our device, we observed an increasing tendency towards developing micro-cracks and a decreasing tendency towards micro-buckles. For instance, 5 nm Ti adhesion layers gave rise to micro-cracked structures on ~1 mm thick PDMS substrates, while buckles formed on PDMS substrates of 60 μm and less; see Fig. S5–S7.†

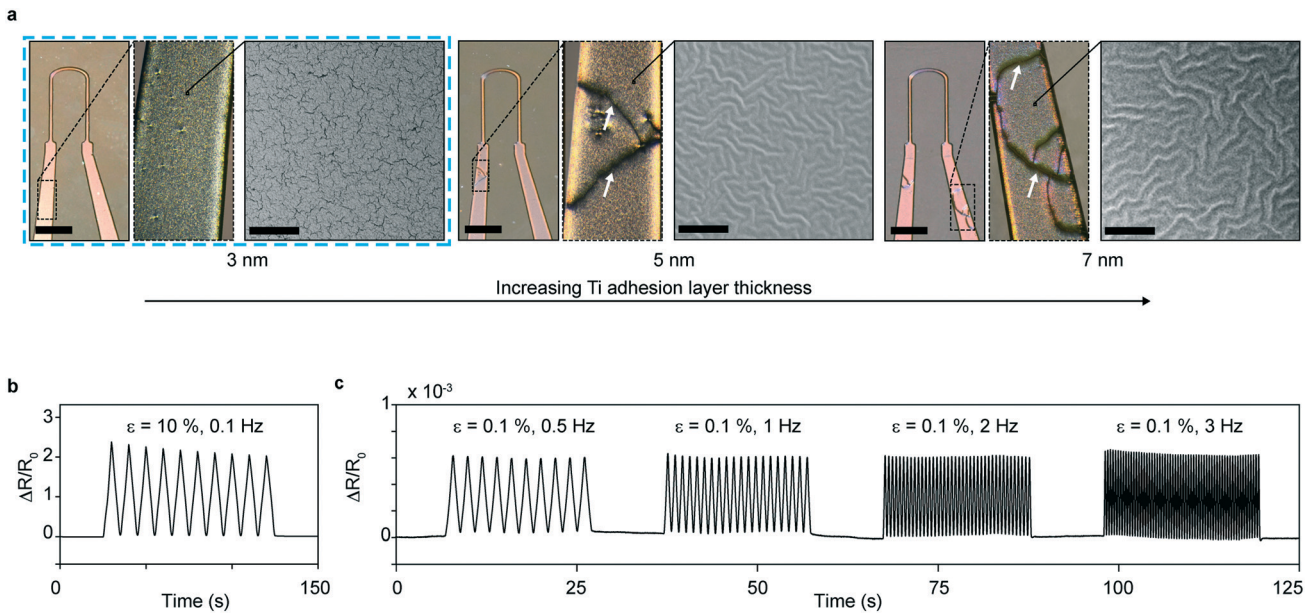

Fig. 2 Titanium–gold thin-film micro-structure, appearance and mechanical robustness. (a) Optical micrographs (left, scale bars 2 mm) and SEM images (right, scale bars 5 μm) of 20 nm Au thin films deposited using 3, 5 or 7 nm Ti adhesion layers, on 5 μm thick PDMS substrates. For 5 nm and 7 nm Ti adhesion layers, buckled micro-structures were observed. These micro-buckled films frequently displayed macroscopic failure cracks in device formulations, deposited through shadow masks. For all thin films applied in devices, 1 nm Ti was added onto Au surface to ensure adhesion to subsequent PDMS layers. Thus, in final devices 3 nm Ti, 20 nm Au, and 1 nm Ti was deposited sequentially. These films yielded robust and reproducible devices. (b and c) Uniaxial strain tests of 3–20–1 nm Ti–Au–Ti thin films deposited on 5 μm thick PDMS substrates. (b) Cyclic 10% strain did not lead to failure in thin-film conductivity. (c) Cyclic strain in the 0.1% regime relevant to the final devices, displayed negligible dependency on strain rate, in the frequency range of tissue contractions.

It is not clear how the PDMS substrate thickness might affect the thin-film micro-structure. It is possible that our observations may be a result of artifacts or indirect effects such as minor changes in surface properties.[21] Previously, the two types of micro-structure have been attributed to whether the Au layer grows on a continuous or discontinuous Ti layer.[21] Buckled thin films were attributed to growth on continuous adhesion layers and micro-cracked thin films were attributed to thinner adhesion layers with a lower degree of PDMS coverage.[21] We propose that the degree of coverage of the Ti adhesion layer may be affected by the PDMS substrate thickness, potentially as part of a lateral edge effect.

Sensor characterization & device readout

To enable conversion of the thin-film strain gauge readout to the contractile stresses generated by the engineered cardiac muscle tissues, we conducted electromechanical and optical characterization of the device components. Initially, we applied a series of uniaxial strain tests to determine the relationship between sensor wire strain and resistance. By comparing these tests with the readouts obtained in the MTF experiments, we found the sensor strains occurring upon tissue contraction to be in the order of 0.1%. Our uniaxial strain tests indicate that in this regime, the micro-cracked thin films display an approximately linear strain–resistance relationship with an apparent gauge factor of 0.6, see Fig. 3a and b and Fig. S8 and S9.† This low gauge factor arises from a significant part of the in-plane strain being relaxed in the form of out-of-plane displacements and rotations of the micro-cracked thin film.[20] However, these modes of relaxation are essential to the operation of the device since they make the thin-film gauges more compliant.

Subsequently, we applied optical tracking to determine the relationship between the curvature of the cantilever and the resistance signal, generally finding a satisfactory correspondence between electrical and optical signal, see Fig. 3c and d and Fig. S10–S14.† Importantly, the sensor readout showed a high degree of repeatability across multiple cantilevers from independent fabrication runs; see Fig. S11–

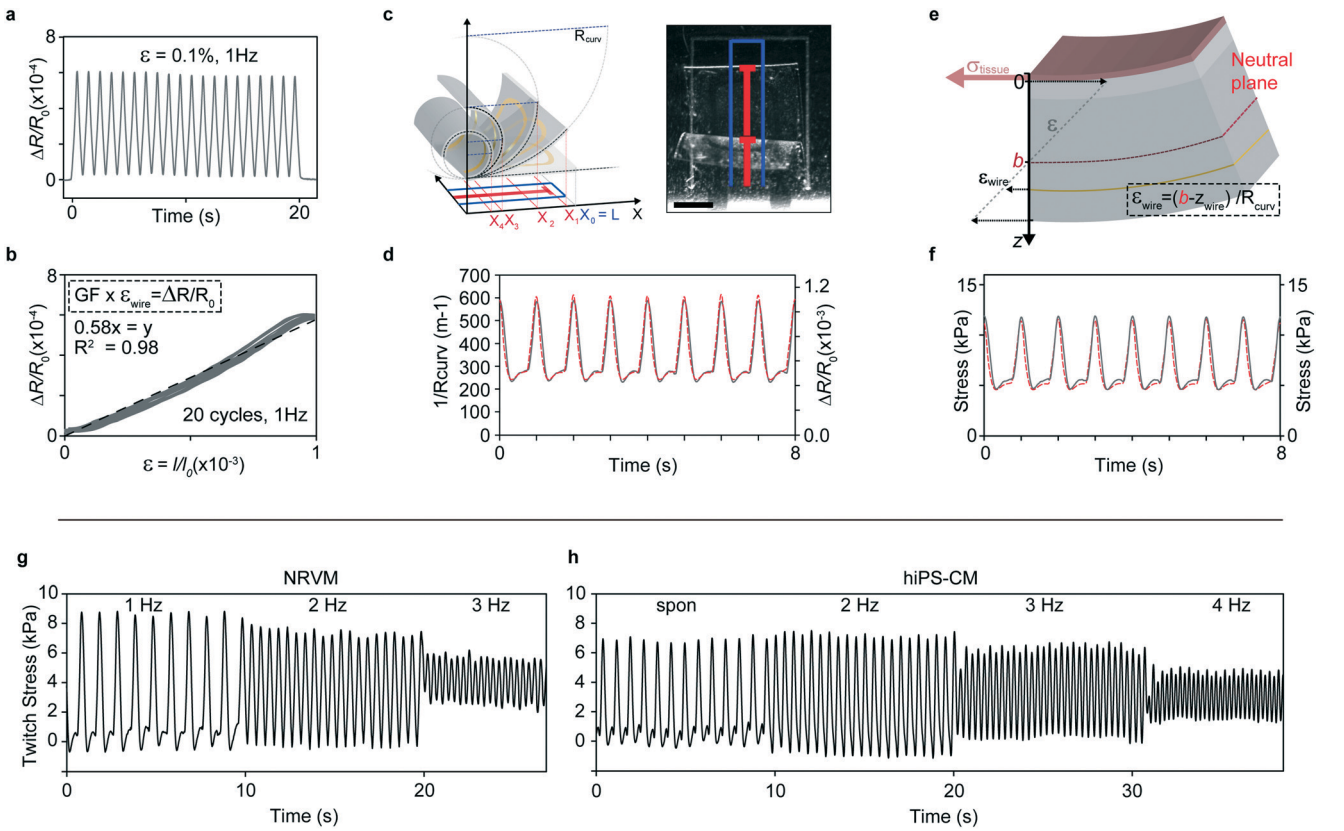

Fig. 3 Thin-film sensor calibration and device mechanical model. (a) Relative resistance change of 3–20–1 nm Ti–Au–Ti thin films deposited on 5 μm PDMS substrates, upon cyclic 0.1% uniaxial strain at 1 Hz. (b) Relative resistance change *vs.* strain for cyclic 0.1% uniaxial strain at 1 Hz. Linear fit (dashed line) indicate a gauge factor (GF) of app. 0.58. (c) Optical tracking of cantilever deflection, scale bar 2 mm. (d) Concurrent optical tracking of cantilever curvature (left axis, dashed red line) and electrical readout of relative resistance change (right axis, solid grey line) from cantilever with NRVM tissue. (e) Principle sketch of mechanical model based on Stoney's equation, applied to convert electrical and optical readout to stress generated by the engineered muscle tissues. By taking advantage of the concurrent optical and electrical readout, the placement of cantilever neutral axis *b* could be determined, see ESI.† (f) Stress values obtained applying mechanical model to convert optical (left axis, dashed red line) and electrical (right axis, solid grey line) readouts displayed in (d) to tissue stress values. (g) Force-frequency of twitch stress of NRVM-based tissues, paced at 1, 2, 3 Hz at day 4 after seeding on devices. (h) Force-frequency of twitch stress of hiPS-CM tissues, spontaneously contracting and paced at 2, 3, 4 Hz at day 6 after seeding.

S14.† This indicates that sensor fabrication is consistent and that the sensors are durable, even to week-long exposure to tissue culture environment and repeated cyclic stretching caused by spontaneous tissue contractions. Yet, we did observe minor discrepancies between optical tracking and sensor readout. At times, a sharp decrease in resistance prior to the increase associated with tissue contraction was detected. We attribute this to a brief uniaxial compression of the gauge, before the tissue contraction overcomes the viscous and inertial forces that hinder out of plane movement of the cantilever.[18] Importantly, these brief artifacts did not influence the final tissue twitch stress values.

Finally, to fully describe the multilayer cantilever, we applied a modified version of Stoney's equation; see Fig. 3e and ESI.† Applying this model we estimated the effective Young's modulus of micro-cracked thin film to be ~0.8 GPa and thus significantly lower than the modulus of bulk gold. Most importantly, tissue twitch stress values of 5–10 kPa were obtained for NRVM MTFs, in very good agreement with previous findings;[10,18] see Fig. 3f and Fig. S13.† We further evaluated the force frequency relationship of the engineered tissues, finding that both hiPS and NRVM MTFs displayed negative force-frequency relationships, indicative of some degree of immaturity;[23] see Fig. 3g and h. Noting that, also for the higher frequencies, we observed a good correspondence between sensor readout and an optical tracking; see Fig. S12.†

Instrumented 24-well platform

The integrated electrical readouts facilitate scaling up the number of assays that can be run in parallel. Our platform allows the contractile stress and beat rate of up to 24 biological replicates to be continuously evaluated, see Fig. 4 and Fig. S15–17.† The wells of the device were made from machined polycarbonate. This limits the total volume of PDMS per well to the cantilever itself, (<0.5 μl volume) thereby reducing concerns related to absorption of hydrophobic drugs.[24] Using a custom recording setup and electrical pacing inserts, the devices facilitate running multiple parallel drug dose–response studies with replicates and references, inside an incubator; see Fig. 4 and Fig. S15–17.†

Cardiac drug dose–response studies

To demonstrate the value of the devices for toxicology and drug screening purposes, we performed sequential dose–response studies of 12 diverse drugs on engineered human cardiac muscle tissues, based on hiPS-CMs. The drugs were chosen to cover a range of cardiac functionalities, and their relative effects on spontaneous peak twitch stress as well as

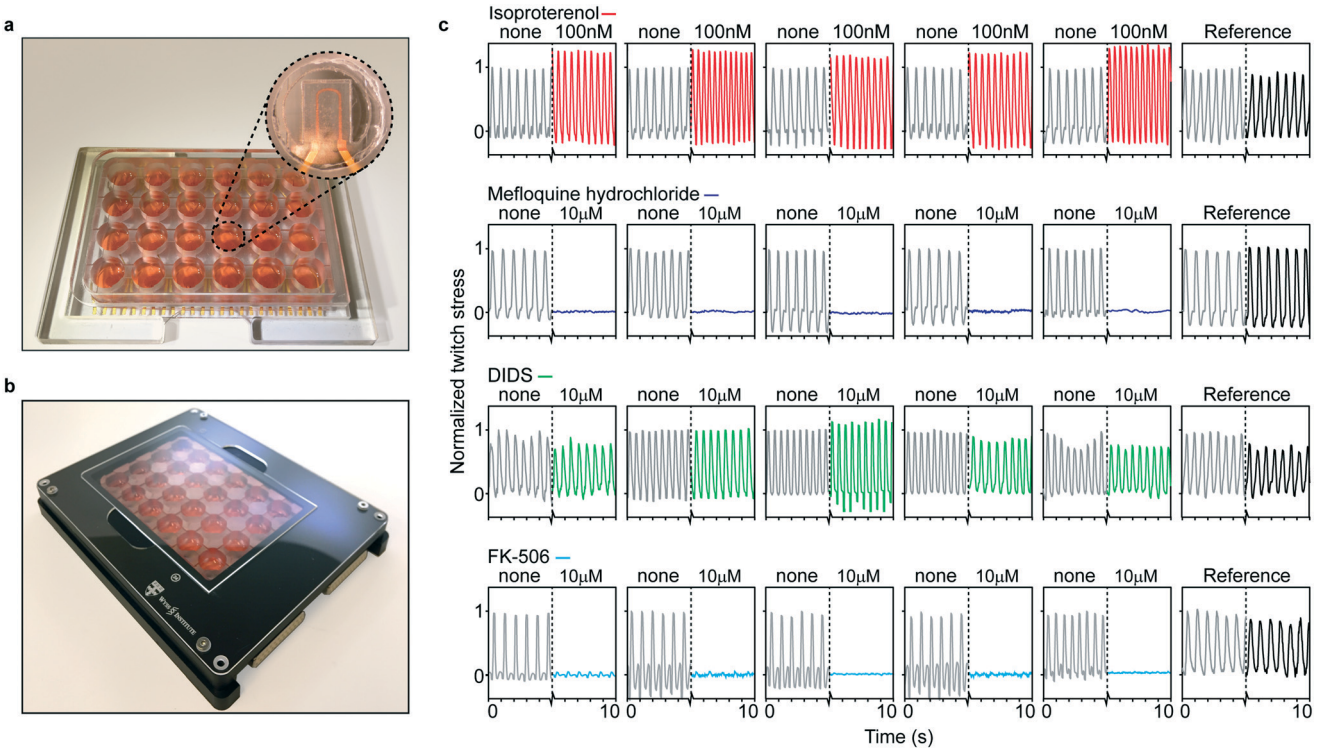

Fig. 4 Instrumented 24-well platform enables multiple parallel experiments. (a) Example 24-well device, with polycarbonate multi-well housing. Insert: Example cantilever in well. (b) 24-Well device in recording holder applied for data acquisition inside incubator environments. (c) 24 example readouts of hiPS-CM tissues applied in drug dose–response experiments, with parallel replicates and references. From top: 100 nM isoproterenol increased beat rate and spontaneous contractile stress, 10 μM mefloquine hydrochloride completely disrupted contraction, 10 μM disodium 4,4′-diisothiocyanatostilbene-2,2′-disulfonate (DIDS) did not cause any notably effects, 10 μM FK-506 markedly decreased contractile stress, but not beat rate.

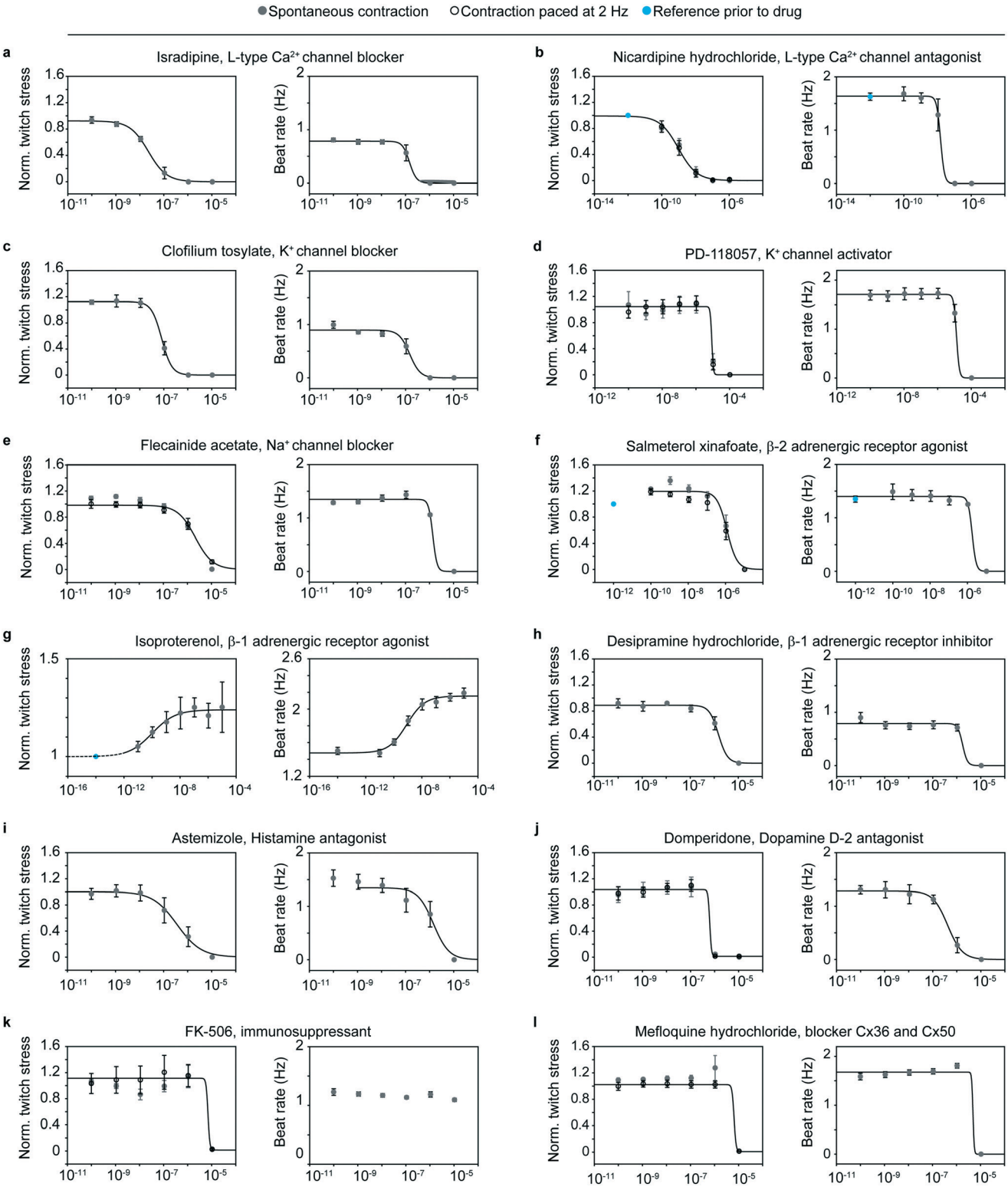

Fig. 5 Sequential drug dose–response studies on hiPS-CM-derived tissues. Increasing drug doses were sequentially added, and tissue spontaneous beat rate and spontaneous twitch stress normalized to initial twitch stress, were recorded (grey circles). For a subset of the studies, the twitch stress while pacing electrically at 2 Hz (hollow circles) was also acquired. Error bars are S.E.M. Lines indicated 4-parameter logistic fits. EC/IC_{50} values obtained from fits are presented in Table 1. (a) Isradipine, $N = 5$ (b) nicardipine, $N = 4$, (c) clofilium tosylate, $N = 5$, (d) PD-118057, $N = 5$, (e) flecanide acetate, $N = 5$, (f) salmeterol xinafoate, $N = 5$, (g) isoproterenol, $N = 6$, (h) desipramine hydrochloride $N = 4$, (i) astemizole $N = 5$, (j) domperidone $N = 5$, (k) FK-506, $N = 5$, (l) mefloquine hydrochloride $N = 5$.

on spontaneous beat rate were studied; see Fig. 5 and Table 1. For a subset of drugs the peak twitch stress for contractions paced at 2 Hz were also acquired.

Ca^{2+}-Channel antagonists are commonly used for treatment of hypertensive diseases.[25] We studied two types of Ca^{2+}-channel blockers: isradipine and nicardipine; see Fig. 5a and b. Both drugs decreased the twitch stress and spontaneous beat rate of the tissues, and both drugs affected twitch stress at 10-fold lower doses than beat rate. We obtained notably higher IC_{50} values for israpidine than nicardipine; see Table 1. This relative difference in potency between the drugs, as well as the range of IC_{50} values, are in accordance with previous studies on human papillary cardiac muscle strips.[25]

Drugs targeting Na^+ and K^+ channels have classically been used for treatment of arrhythmias, but carry an inherent dose-dependent proarrhythmic risk.[26,27] At the same time, off-target interaction with hERG K^+-channel is a most common concern in drug development, due to the risk of inducing ventricular arrhythmias, fibrillation and torsades de pointes (TdP).[28] We tested hERG K^+-channel blocker clofilium tosylate, Fig. 5c, and the activator PD-118057, Fig. 5d. For clofilium we observed a disruption of spontaneous contraction as indicated by a drop in beat rate and twitch stress with IC_{50} in the 100 nM range; see Table 1, matching the range previously found to induce TdP in isolated rabbit heart models *in vitro*.[29] For PD-118057 we observed a disruption of spontaneous beat rate and twitch stress in the 10 μM range. Interestingly, previous *in vitro* electrophysiological evaluations of induced stem cell-derived cardiomyocytes carrying a long QT syndrome type 2 mutation found that a slightly lower dose decreased action potential (AP) duration and rescued early after-depolarisation events.[30] We also perturbed Na^+-channels through exposure to flecainide acetate, observing a simultaneous drop in spontaneous beat rate and twitch stress in the single μM range; see Fig. 5e and Table 1, illustrating the well-established risks associated with flecainide.[26,31]

Table 1 EC_{50} or IC_{50} values from sequential drug dose–response studies on hiPS-CM-derived tissues. Values obtained from 4-parameter logistic fits to data presented in Fig. 5. (spon): from spontaneous twitch stress (paced): from twitch stress while pacing electrically at 2 Hz

EC_{50} or IC_{50}	Twitch stress	Spontaneous beat frequency
Isradipine	22.5 nM (spon)	147 nM
Nicardipine	1.19 nM (spon), 0.971 nM (paced)	15.2 nM
Clofilium	81.6 nM (spon)	148 nM
PD-118057	8.8 μM (spon), 8.77 μM (paced)	13.3 μM
Flecainide	1.37 μM (spon), 2.12 μM (paced)	1.37 μM
Salmeterol	1.07 μM (spon), 1.08 μM (paced)	1.79 μM
Isoproterenol	0.107 nM (spon)	0.844 nM
Desipramine	1.49 μM (spon)	1.75 μM
Astemizole	0.361 μM (spon)	1.44 μM
Domperidone	0.731 μM (spon), 0.629 μM (paced)	0.419 μM
FK-506	7.15 μM (spon), 7.00 μM (paced)	—
Mefloquine	2.18 μM (spon), 6.48 μM (paced)	1.44 μM

Given the central role of adrenergic receptors in regulating cardiac rate and contractile strength, we studied the effect of a β-2 agonist: salmeterol xinafoate and a β-1 agonist: isoproterenol; see Fig. 5f and g and Table 1. For salmeterol xinafoate, we observed a minor increase in twitch stress at low doses, in agreement with the canonical effects of β-2 agonists. At higher doses, we observed a cardiotoxic effect marked by stress and beat rate reduction in the μM range. A cardiotoxic effect at higher doses has previously been observed for hiPS-CM *in vitro*.[32] For the β-1 agonist isoproterenol we observed well-described increases in spontaneous beat rate and spontaneous twitch stress with EC_{50} in the 0.1–1 nM range, comparable, while slightly lower than our previous studies on hiPS-CM based tissues,[18] and studies by other groups of *in vitro* engineered cardiac stem cell-derived tissues.[33]

We additionally tested several non-cardiac drugs with severe cardiotoxic side effects. The antidepressant desipramine has been associated with fatal arrhythmias in several children.[34] For this drug, we observed an arrest of spontaneous contraction in the single μM range; see Fig. 5h and Table 1. Astemizole is a histamine antagonist which was withdrawn due to hERG blockade side effects.[35] For astemizole we found that the spontaneous beating and stress were disrupted in the single μM range; see Fig. 5i and Table 1. For the dopamine receptor agonist domperidone, which has previously been found to induce arrhythmia and sudden cardiac death side effects,[36] we observed a concerted disruption in tissue beat rate and contractile stress in the 0.5 μM range; see Fig. 5j and Table 1. FK-506 is an immunosuppressant used in organ transplants to prevent transplant rejection, with calcineurin-related hypertension and hypertrophy cardiac side effects.[37,38] For this drug, we observed a diminished contractile stress in the 10 μM range, with no apparent influence on beat rate; see Fig. 5k and Table 1. Finally, for the malarial drug mefloquine, a range of cardiac side effects including arrhythmia and inotropic side effects have been reported.[39,40] For this drug, we observed an abrupt drop in both contractile stress and rate at μM doses; see Fig. 5l and Table 1. Collectively, the drug dose–response studies demonstrate the ability of the platform to detect a range of cardiac effects and side-effects on human stem cell-derived tissues, in a higher-throughput manner.

Cardiac drug exposure through endothelial barrier inserts

The standard open-well format of our instrumented cardiac platform makes it compatible with a range of common laboratory tools such as Transwell® inserts, which can support endothelial tissue barriers; see Fig. 6a. The endothelium of the vasculature plays a critical role in regulating molecular transport to the heart musculature.[13,15] Changes in endothelium permeability such as those occurring during inflammation can thus have a pronounced influence on the transport of cardiac drugs.[13,14] To mimic such events, we studied the transport and subsequent cardiac effect of the Ca^{2+} channel blocker Isradipine, across a vascular endothelial barrier with and without co-exposure of TNF-α.[16]

We added a high Isradipine dose, 100 nM, to the insert containing media and a confluent endothelial monolayer, and studied the passive transport across the barrier by evaluating the contractile stress of the cardiac MTFs below. As expected, the barrier significantly delayed the cardiac response to the drug, see Fig. 6b and c. While direct exposure of the drug immediately disrupts the contractile function of the cardiac tissue, contractile function remains only partially affected after 8 h and fully disrupted after 20 h, when protected by the endothelial barrier. Notably, this temporal profile can be altered by disrupting the endothelial barrier using TNF-α, a potent regulator of vascular permeability *in vivo*.[16] TNF-α accelerated the passive transport of Isradipine across the endothelial tissue as evident by a complete disruption of contractile function being observed after 5.5 h; see Fig. 6b. TNF-α alone did not decrease the contractile stress; see Fig. 6c. We noted that the effect of TNF-α on endothelial barrier function was evident only after 4 hours of co-exposure. As control, we confirmed this response time by studying the effect of TNF-α isolated endothelial barriers; see Fig. 6d and f and Fig. S18.† Collectively, these studies demonstrate how the complexity of the assay can be increased to include aspects of drug transport, delivery and co-administration as well as paracrine signaling effects.[41]

General discussion

An inherent dilemma for MPS and organs-on-chips aimed at pharmaceutical applications is how to balance high biological content *versus* high experimental throughput. This tradeoff is reflected in multifarious approaches that have been taken in studying human stem cell-derived cardiomyocytes and engineered cardiac tissues. These range from construction of thicker 3D constructs,[33,42–45] some even with embedded vasculatures,[46] to 2D single cell and cell-pair islands.[47] The extremities each hold value and drawbacks. For instance, increasing size and complexity of model tissue can simultaneously increase the amount of cells required and challenges associated with fabrication.[44,48,49] Similarly, 2D cell islands offer closely defined geometry, mechanical and chemical cellular environment, at the expense of tissue ensemble effects. Whether following a predominantly holistic or reductionist approach, a central challenge is capturing essential structural and functional hallmarks of the native counterpart in question. MTFs are inherently 2D with cell–cell connections being confined to a single plane, and do not support the incorporation of vasculature. Accordingly, studying effects such as drug diffusion through the tissue will require the use of a thicker model tissue. Yet, MTFs replicate the laminar structure, electrical connectivity and anisotropy

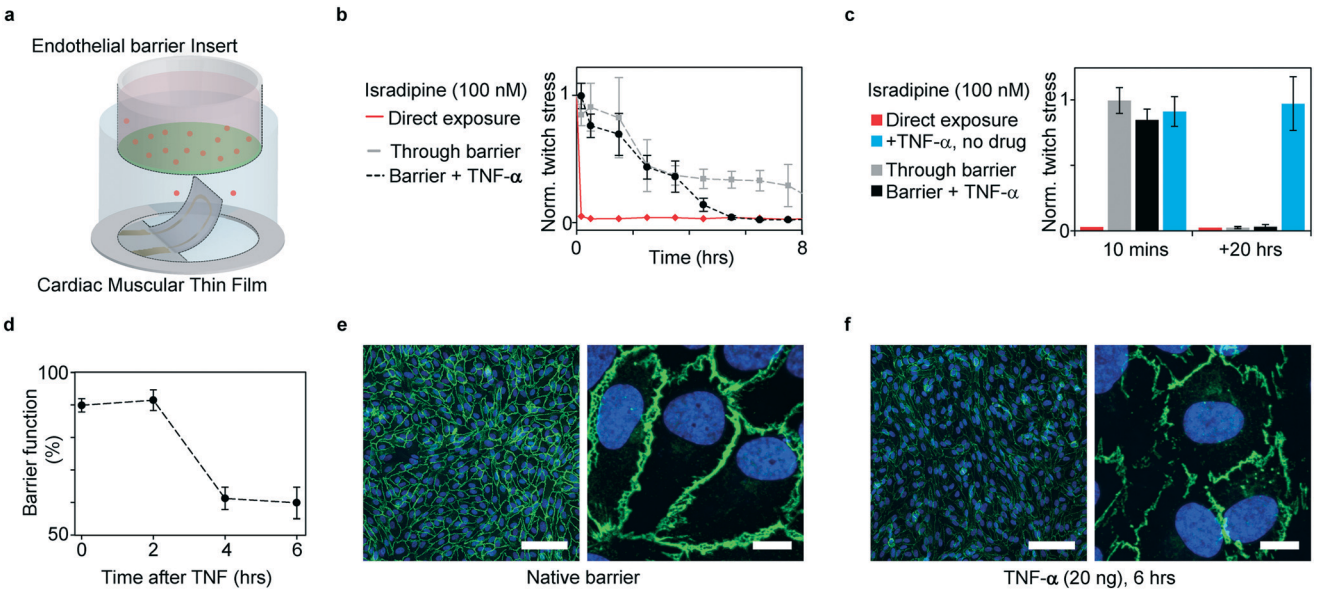

Fig. 6 Coupling endothelial barriers with cardiac MTFs to study drug transport. (a) Schematic illustration of experiments. Endothelial barrier tissues in Transwell® inserts are introduced into the wells of the instrumented cardiac 24-well MTF platform. A cardiac drug (isradipine) is introduced in the volume shielded by the endothelial barrier. Drug transport across barrier and resultant cardiac effects are recorded in real-time through embedded sensors. (b) Decrease in normalized contractile twitch stress over time. Direct exposure of isradipine (100 nM) immediately halts contraction (red). Exposure of isradipine (100 nM) through endothelial barrier inserts (grey line), leads to delayed drug effect, where contraction is still observed after >7 h exposure. (N = 3). Compromising endothelial barrier function by co exposure with TNF-α significantly accelerates drug diffusion, leading to a full effect of the drug after ~5 h. (c) After 20 h full effect of isradipine was observed for all samples. TNF-α did not directly introduce changes in twitch stress of cardiac tissues. (d) Endothelial tissue barrier function decreases upon exposure to TNF-α (20 ng ml^{-1}). Barrier function was evaluated as percent of fluorescent marker (400 Da) contained inside barrier during 20 min diffusion into reservoir without tracer. (e) Confocal microscopy of immunostained intact endothelial barrier. Blue: DAPI nuclei stain, green: VE-cadherin, scale bars left: 100 μm, right: 10 μm. (f) Confocal microscopy of immunostained endothelial barrier after exposure to 20 ng ml^{-1} TNF-α for 6 h. Blue: DAPI nuclei stain, green: VE-cadherin, scale bars left: 100 μm, right: 10 μm.

of the heart musculature. Further, the soft cantilever substrates allow the tissue to shorten, similarly to in the native heart. In this report, we studied the responses of cardiac MTFs based on human induced stem cells, to 12 diverse cardiac drugs. Our findings largely match prior *in vivo*, *ex vivo* and engineered tissue findings, demonstrating the relevance of human cardiac MTFs for drug screening and toxicology applications.

Beyond considering the biological complexity of the model tissues, data acquisition considerations are of critical and often overlooked importance when aiming to scale MPS to the large numbers required for drug screening and toxicology applications. Integration of appropriate sensors represents an appealing route to scaling up the number of assays that can be run in parallel. However, sensor integration increases fabrication complexity, in particular since structure and function of tissue models should not be disrupted. Consequently, instrumented MPS that take advantage of electronic readouts to provide higher throughputs assays have only recently started to emerge.[18,50] The 2D structure of MTF cardiac model tissues facilitates integration of strain gauges sensors while only minimally increasing fabrication complexity.

The micro-cracked titanium–gold thin films offer a number of benefits as sensor material for this application. In addition to a repeatable and scalable fabrication procedure, the sensors display a high degree of robustness, with no significant changes being observed during culture, and with similar sensitivity across independent cantilevers. The stretchability of the micro-cracked thin films additionally reduced the bending stiffness of the cantilevers; ensuring tissues were not hindered in contractile shortening. Yet, the micro-cracks also represent a draw-back as they are the central cause behind the relatively low gauge factor of the sensors. Alternative sensor materials such as soft composites based on elastomers with conducting particle additives are interesting alternatives, due to their low stiffness and high sensitivities.[18,51]

Conclusions

In this report, we addressed key challenges associated with scaling cardiac microphysiological systems to the high throughputs required for preclinical and toxicological research. We demonstrated how incorporation of flexible thin-film sensors allowed fabrication of a multi-well platform with continuous readout of the contractile stress and beat rate of up to 24 human stem cell-derived engineered cardiac tissues. The platform significantly simplifies drug tests, which we demonstrated by performing full dose–response studies of 12 cardiac and cardiotoxic drugs. Further, the open-well design of the platforms ensured compatibility with a range of standard laboratory tools, to enable coupled studies of cardiac drug transport across human vascular endothelial barriers inserts. The platform fabrication relies on generally accessible, scalable techniques, and on robust micro-cracked Ti–Au thin films for sensing. The methodology presented in this report is thus generally applicable and well-suited for cardiac drug screening and disease modelling purposes. It therefore provides a path towards high-throughput, high-quality preclinical research, based on human stem-cell derived cardiac tissues.

Materials & methods

Device fabrication

24-Well devices were fabricated on 127.9 mm × 85.8 mm × 1.0 mm glass substrates, following a bottom-up procedure. First, silver contact pads on the device edge were made by stencil printing of AG-510 from Conductive Compounds, annealing at 190 °C for 30 min. Subsequently, poly(*N*-isopropylacrylamide) (PNIPAAM) release layer islands were made using a pressure sensitive pen to dispense 2 w/v% solution in isopropanol or by masked spin coating of a 10 w/v% PNIPAAM solution in 1-butanol. Subsequently, PDMS (Sylgard 184 Dow-Corning) layers were made through stepwise spin-coating and curing overnight at 65 °C. For bottom PDMS either 4000 rpm or 5000 rpm (5 min) were used; equivalent to a 5.2 or 3.3 μm thick layer, respectively. Ti–Au–Ti (3 nm, 20 nm, 1 nm) sensor wires were added using a custom stainless steel shadow mask (NewCut) and an e-beam evaporator (Denton), starting deposition at 0.9–1 × 10^{-6} Torr. To ensure localization of the resistance to the cantilever loop, 100 nm Au, 1 nm Ti was added to the non-cantilever wire parts. Following evaporation, a middle PDMS layer was added by spin-coating at 2000 rpm or 1500 rpm (5 min); equivalent to a 11.9 or 16.2 μm thick layer, respectively. Following curing, thin films were annealed to release pre-stress by heating to 190 °C for 30 min. Lastly, a softer PDMS coating was added by spincoating a 2 : 1 mix of Sylgard 527 and Sylgard 184 (Dow-Corning) at 2500 rpm (5 min); equivalent to a 6.2 μm thick coating. For hiPS-CM devices, the soft PDMS layer was micro-molded (30 μm × 4 μm × 5 μm, gap width × barrier width × barrier height) using fluorinated ((tridecafluoro-1,1,2,2-tetrahydrooctyl)-1-trichlorosilane, United Chem) PDMS stamps. Cantilevers were defined using a CO_2 laser-cutter (Epilog). Milled polycarbonate wells were attached to the device by casting a thin PDMS gasket onto the well part and attaching it to PDMS-covered glass substrate using plasma treatment.

Device cell seeding and tissue culture

Human iPS-CM tissues: fully assembled devices with micro-molded cantilevers were sterilized using UV-ozone. Subsequently, wells were incubated with a 50 μg ml^{-1} solution of human fibronectin (FN, BD Biosciences) in PBS, for at least 1 h. After removal of the FN solution, hiPS-CMs (Cor4U, Axiogenesis, Germany) were seeded at ~200 000 cm^{-2} in designated Commercial Cor4U media (Axiogenesis, Germany). Cor4U media was changed every 2 days.

Neonatal Rat Ventricular Myocyte tissues: non-molded devices were sterilized using UV-ozone. FN line patterns (15 μm × 4 μm) were micro-contact printed onto cantilevers using previously established procedures.[12] Primary NRVMs were seeded at a density of ~140 000 cm^{-2} in 10% FBS in media 199 (Lonza). Cell media was replaced every 2 days, applying

2% FBS in media 199 (Lonza). NRVMs were obtained from newborn Sprague Dawley rats ($n \geq 10$ litters, per harvest) following procedures approved by the Harvard University Animal Care and Use Committee; the Institutional Animal Care and Use Committee (IACUC). The procedures follow "US Government Principles for the Utilization and Care of Vertebrate Animals Used in Testing, Research, and Training", the Guide for the Care and Use of Laboratory Animals 8th Ed., the Animal Welfare Act/Regulations, as well as other federal, state and city laws and regulations.

Endothelial barrier culture

Prior to cell seeding, polycarbonate Transwell® inserts with 0.4 μm pores (Corning) were incubated with 50 μg mL^{-1} human fibronectin (FN, BD Biosciences) in PBS for 2 h and inserts were rinsed twice with PBS. Human umbilical vein endothelial cells (ATCC) were seeded at a density of ~75 000 cm^{-2} in commercial endothelial growth media and supplements containing 2% FBS (Lonza). Media was changed daily and exchanged to reduced serum media containing 0.5% FBS on day 3 and 4.

Data acquisition & stress calculation

Data were acquired using a custom polycarbonate connector and a Keithley Multichannel DMM 3706a. The 2-wire resistance recordings were generally obtained, at sampling rates ≥60 Hz.

To convert the resistance readout to stresses generated by the tissues, we applied a mechanical model based on a modified Stoney's equation. After determining the mechanical properties of each layer in the cantilever, as well as the gauge factor of the Ti–Au thin film, this model provided linear conversion constants between relative changes in resistance and tissue contractile stress; see ESI† for details. Custom MATLAB (MathWorks, Natick, MA) codes were applied for quantifying relative resistance changes as well as for converting to stress. For electrically paced samples, a median filter (5) was applied to filter noise from pacing.

Cumulative drug dose studies

Cumulative dosing of cardiac drugs was performed on engineered hiPS-CM tissues inside incubator at day 6–9 after seeding. 900 μl serum-free media was added to each cell well prior to drug dose experiments. A dilution series of the drugs in media was added in 9 μl doses. Samples were incubated with dose 10 min prior to recording. For each dose, 30 s were recorded per channel. Isoproterenol stocks were kept at 4 °C prior to dosing. Pacing was applied using custom platinum wire electrodes. Each n in analysis denotes biological replicate of a tissue in separate isolated well with associated sensor and media. Drugs were obtained from Sigma-Aldrich (LO2219).

Endothelial barrier testing and disruption

Barrier function tests were performed using Oregon Green 488 carboxylic acid (~412 Da) and Alexa Fluor 555 succinimidyl ester (~1250 Da) as fluorescent tracers (ThermoFisher). Fluorescent media containing 1 μg ml^{-1} of each tracer was added to the top insert and incubated for 20 min. Samples of top and bottom media were collected and fluorescent intensity was measured using a Synergy HT plate reader (BioTek) to estimate barrier permeability. Barrier function was calculated as percent tracer contained in top reservoir. To disrupt barrier function, human tumor necrosis factor alpha (Sigma-Aldrich) was diluted in endothelial media to a concentration of 20 ng mL^{-1} and was added to inserts. Fluorescent intensity of top and bottom media was measured every 2 h to estimate barrier disruption over the course of 6 h.

Tissue immuno-staining and OOP structural analysis

All immunocytochemistry procedures were conducted at room temperature. Cardiac samples were fixed with 4% PFA/PBS (v/v) solution for 10 min and then permeabilized with 0.05% Triton-X/PBS (v/v) solution for 10 min. Subsequently, samples were incubated for 1 h with monoclonal sarcomeric α-actinin (clone EA-53; Sigma-Aldrich) and Cx43 (ab11370; abcam) primary antibodies, washed three times in PBS, and finally counterstained with Alexa Fluor 488-conjugated anti-mouse secondary antibody and Alexa Fluor 546-conjugated anti-rabbit secondary antibody, Alexa Fluor 633-conjugated Phalloidin and DAPI (Invitrogen). Endothelial barrier tissues were fixed using with 4% PFA/PBS (v/v) for 10 min and permeabilized using 0.05% Triton-X/PBS (v/v) solution for 2 min. Subsequently, samples were incubated with 5% bovine serum albumin/PBS (w/v) for 30 min and washed three times in 0.5% BSA/PBS (w/v). Samples were incubated for 1 h with rabbit polyclonal antibody to VE-cadherin (Abcam, ab33168) and mouse monoclonal antibody to CD31 (PECAM) (Abcam, ab24590) and rinsed three times with 0.5% BSA/PBS. Samples were counterstained for 2 h with Alexa Flour 488-conjugated anti-rabbit secondary antibody, Alexa Fluor 546-conjugated anti-mouse secondary antibody, and DAPI (ThermoFisher) and rinsed three times with 0.5% BSA/PBS. Samples were mounted on coverslips using ProLong Gold Antifade (ThermoFisher). Samples were imaged using confocal microscopy (Olympus) and z-stacks were projected to acquire images of cardiac tissues and endothelial barriers. The alignment and spatial organization of α-actinin positive structures were evaluated using the OOP methodology, previously described.[19] Briefly, for both NRVM and hiPS-CM tissues, z-stacks of this sarcomere stain was acquired for 5 independent FOVs (from at least 3 samples). Following z-projection, the angular orientation of all sarcomeres was calculated and the degree of similarity in their orientations was quantified in terms of their OOP using a custom MATLAB (MathWorks, Natick, MA) code.[19]

Conflicts of interest

There are no conflicts to declare.

Acknowledgements

This work was performed in part at the Center for Nanoscale Systems (CNS), a member of the National Nanotechnology Coordinated Infrastructure Network (NNCI), which is supported by the National Science Foundation under NSF award no. 1541959. CNS is part of Harvard University. Research reported in this publication was supported by the National Center for Advancing Translational Sciences of the National Institutes of Health under Award Number UH3TR000522; U. S. Army Research Laboratory and the U. S. Army Research Office under Contract No. W911NF-12-2-0036; and the Harvard University Materials Research Science and Engineering Center (MRSEC), NSF Award number DMR-1420570. The views and conclusions contained in this document are those of the authors and should not be interpreted as representing the official policies, either expressed or implied, of the Army Research Office, Army Research Laboratory, the U.S. Government or the National Institutes of Health. The U.S. Government is authorized to reproduce and distribute reprints for Government purposes notwithstanding any copyright notation hereon. Authors thanks K. Hudson and M. Rosnach for assistance with photography, as well as J. Ferrier and A. Cho for their assistance with 3D rendering and shadow-mask fabrications. Authors additionally thank F. S. Pasqualini, S. P. Sheehy, J. A. Goss, T. A. Busbee and T. Biering-Sorensen for helpful discussions.

References

1 A. D. Schachter and M. F. Ramoni, *Nat. Rev. Drug Discovery*, 2007, **6**, 107–108.
2 J. A. DiMasi, H. G. Grabowski and R. W. Hansen, *J. Health. Econ.*, 2016, **47**, 20–33.
3 H. Olson, G. Betton, D. Robinson, K. Thomas, A. Monro, G. Kolaja, P. Lilly, J. Sanders, G. Sipes and W. Bracken, *Regul. Toxicol. Pharmacol.*, 2000, **32**, 56–67.
4 A. S. Go, D. Mozaffarian, V. L. Roger, E. J. Benjamin, J. D. Berry, M. J. Blaha, S. Dai, E. S. Ford, C. S. Fox and S. Franco, *Circulation*, 2013, **127**, e62–e245.
5 G. D. Buckberg, J. I. Hoffman, H. C. Coghlan and N. C. Nanda, *Eur. J. Cardiothorac. Surg.*, 2015, **47**, 587–601.
6 M. J. Kocica, A. F. Corno, F. Carreras-Costa, M. Ballester-Rodes, M. C. Moghbel, C. N. Cueva, V. Lackovic, V. I. Kanjuh and F. Torrent-Guasp, *Eur. J. Cardiothorac. Surg.*, 2006, **29**, S21–S40.
7 I. J. LeGrice, B. Smaill, L. Chai, S. Edgar, J. Gavin and P. J. Hunter, *Am. J. Physiol. Heart Circ. Physiol.*, 1995, **269**, H571–H582.
8 A. W. Feinberg, A. Feigel, S. S. Shevkoplyas, S. Sheehy, G. M. Whitesides and K. K. Parker, *Science*, 2007, **317**, 1366–1370.
9 A. Grosberg, P. W. Alford, M. L. McCain and K. K. Parker, *Lab Chip*, 2011, **11**, 4165–4173.
10 M. L. McCain, A. Agarwal, H. W. Nesmith, A. P. Nesmith and K. K. Parker, *Biomaterials*, 2014, **35**, 5462–5471.
11 G. Wang, M. L. McCain, L. Yang, A. He, F. S. Pasqualini, A. Agarwal, H. Yuan, D. Jiang, D. Zhang and L. Zangi, *Nat. Med.*, 2014, **20**, 616–623.
12 A. Agarwal, J. A. Goss, A. Cho, M. L. McCain and K. K. Parker, *Lab Chip*, 2013, **13**, 3599–3608.
13 L. González-Mariscal, P. Nava and S. Hernandez, *J. Membr. Biol.*, 2005, **207**, 55–68.
14 C. B. Henry and B. R. Duling, *Am. J. Physiol. Heart Circ. Physiol.*, 2000, **279**, H2815–H2823.
15 D. Tirziu, F. J. Giordano and M. Simons, *Circulation*, 2010, **122**, 928–937.
16 J. A. Royall, R. L. Berkow, J. S. Beckman, M. K. Cunningham, S. Matalon and B. A. Freeman, *Am. J. Physiol. Lung Cell Mol. Physiol.*, 1989, **257**, L399–L410.
17 K. K. Parker, J. U. Lind, J. A. Lewis, J. J. Vlassak, H. Yuan, T. A. Busbee, I. Perkins and C. Chantre, *US Pat. App*, 20170016875A1, WO2015178980A3, 2017.
18 J. U. Lind, T. A. Busbee, A. D. Valentine, F. S. Pasqualini, H. Yuan, M. Yadid, S.-J. Park, A. Kotikian, A. P. Nesmith and P. H. Campbell, *Nat. Mater.*, 2017, **16**, 303–308.
19 F. S. Pasqualini, S. P. Sheehy, A. Agarwal, Y. Aratyn-Schaus and K. K. Parker, *Stem Cell Rep.*, 2015, **4**, 340–347.
20 S. P. Lacour, D. Chan, S. Wagner, T. Li and Z. Suo, *Appl. Phys. Lett.*, 2006, **88**, 204103.
21 O. Graudejus, P. Görrn and S. Wagner, *ACS Appl. Mater. Interfaces*, 2010, **2**, 1927–1933.
22 I. M. Graz, D. P. Cotton and S. P. Lacour, *Appl. Phys. Lett.*, 2009, **94**, 071902.
23 M. Endoh, *Eur. J. Pharmacol.*, 2004, **500**, 73–86.
24 M. W. Toepke and D. J. Beebe, *Lab Chip*, 2006, **6**, 1484–1486.
25 R. H. Schwinger, M. Böhm and E. Erdmann, *J. Cardiovasc. Pharmacol.*, 1990, **15**, 892–899.
26 D. S. Echt, P. R. Liebson, L. B. Mitchell, R. W. Peters, D. Obias-Manno, A. H. Barker, D. Arensberg, A. Baker, L. Friedman and H. L. Greene, *N. Engl. J. Med.*, 1991, **324**, 781–788.
27 S. H. Hohnloser, *Am. J. Cardiol.*, 1997, **80**, 82G–89G.
28 J.-P. Valentin and T. Hammond, *J. Pharmacol. Toxicol. Methods*, 2008, **58**, 77–87.
29 L. Eckardt, W. Haverkamp, H. Mertens, R. Johna, J. R. Clague, M. Borggrefe and G. Breithardt, *J. Cardiovasc. Pharmacol.*, 1998, **32**, 425–434.
30 E. Matsa, D. Rajamohan, E. Dick, L. Young, I. Mellor, A. Staniforth and C. Denning, *Eur. Heart J.*, 2011, **32**, 952–962.
31 U. Borchard and M. Boisten, *J. Cardiovasc. Pharmacol.*, 1982, **4**, 205–212.
32 O. Sirenko, E. F. Cromwell, C. Crittenden, J. A. Wignall, F. A. Wright and I. Rusyn, *Toxicol. Appl. Pharmacol.*, 2013, **273**, 500–507.
33 D. Zhang, I. Y. Shadrin, J. Lam, H.-Q. Xian, H. R. Snodgrass and N. Bursac, *Biomaterials*, 2013, **34**, 5813–5820.
34 P. Pacher and V. Kecskemeti, *Curr. Pharm. Des.*, 2004, **10**, 2463–2475.
35 Z. F. Zhou, V. R. Vorperian, Q. M. Gong, S. T. Zhang and C. T. January, *J. Cardiovasc. Electrophysiol.*, 1999, **10**, 836–843.

36 C. B. Johannes, C. Varas-Lorenzo, L. J. McQuay, K. D. Midkiff and D. Fife, *Pharmacoepidemiol. Drug Saf.*, 2010, **19**, 881–888.
37 P. Atkison, G. Joubert, A. Barron, D. Grant, K. Paradis, E. Seidman, W. Wall, H. Rosenberg, J. Howard, S. Williams and C. Stiller, *Lancet*, 1995, **345**, 894–896.
38 L. W. Miller, *Am. J. Transplant.*, 2002, **2**, 807–818.
39 W. Fonteyne, A. Bauwens and L. Jordaens, *Clin. Cardiol.*, 1996, **19**, 967–968.
40 S. J. Coker, A. J. Batey, I. D. Lightbown, M. E. Diaz and D. A. Eisner, *Br. J. Pharmacol.*, 2000, **129**, 323–330.
41 D. L. Brutsaert, *Physiol. Rev.*, 2003, **83**, 59–115.
42 A. F. Godier-Furnémont, M. Tiburcy, E. Wagner, M. Dewenter, S. Lämmle, A. El-Armouche, S. E. Lehnart, G. Vunjak-Novakovic and W.-H. Zimmermann, *Biomaterials*, 2015, **60**, 82–91.
43 W. H. Zimmermann, C. Fink, D. Kralisch, U. Remmers, J. Weil and T. Eschenhagen, *Biotechnol. Bioeng.*, 2000, **68**, 106–114.
44 T. Boudou, W. R. Legant, A. Mu, M. A. Borochin, N. Thavandiran, M. Radisic, P. W. Zandstra, J. A. Epstein, K. B. Margulies and C. S. Chen, *Tissue Eng., Part A*, 2011, **18**, 910–919.
45 N. Thavandiran, N. Dubois, A. Mikryukov, S. Massé, B. Beca, C. A. Simmons, V. S. Deshpande, J. P. McGarry, C. S. Chen and K. Nanthakumar, *Proc. Natl. Acad. Sci. U. S. A.*, 2013, **110**, E4698–E4707.
46 B. Zhang, M. Montgomery, M. D. Chamberlain, S. Ogawa, A. Korolj, A. Pahnke, L. A. Wells, S. Massé, J. Kim and L. Reis, *Nat. Mater.*, 2016, **15**, 669–678.
47 Y. Aratyn-Schaus, F. S. Pasqualini, H. Yuan, M. L. McCain, J. George, S. P. Sheehy, P. H. Campbell and K. K. Parker, *J. Cell Biol.*, 2016, **212**, 389–397.
48 N. Huebsch, P. Loskill, N. Deveshwar, C. I. Spencer, L. M. Judge, M. A. Mandegar, C. B. Fox, T. M. Mohamed, Z. Ma and A. Mathur, *Sci. Rep.*, 2016, **6**, 24726.
49 A. Mathur, P. Loskill, K. Shao, N. Huebsch, S. Hong, S. G. Marcus, N. Marks, M. Mandegar, B. R. Conklin and L. P. Lee, *Sci. Rep.*, 2015, **5**, 8883.
50 M. Odijk, A. van der Meer, D. Levner, H. Kim, M. van der Helm, L. Segerink, J. Frimat, G. Hamilton, D. Ingber and A. van den Berg, *Lab Chip*, 2015, **15**, 745–752.
51 C. S. Boland, U. Khan, G. Ryan, S. Barwich, R. Charifou, A. Harvey, C. Backes, Z. Li, M. S. Ferreira and M. E. Möbius, *Science*, 2016, **354**, 1257–1260.

